Astron. Astrophys. 342, 736–744 (1999)

ASTRONOMY AND ASTROPHYSICS

Evolution of spectral parameters during a pre-eclipse dip of Her X-1⋆

B. Stelzer[1,⋆⋆], **J. Wilms**[1], **R. Staubert**[1], **D. Gruber**[2], **and R. Rothschild**[2]

[1] Institut für Astronomie und Astrophysik – Astronomie, University of Tübingen, Waldhäuser Strasse 64, D-72076 Tübingen, Germany
[2] Center for Astrophysics and Space Sciences, UCSD, La Jolla, CA 92093, USA

Received 29 May 1998 / Accepted 3 November 1998

Abstract. We report on a pre-eclipse dip of the X-ray binary pulsar Her X-1 observed by the Rossi X-ray Timing Explorer (RXTE) in 1996 July. The energy spectra in the 3–18 keV range can be described by the sum of two power-laws, one of which is modified by photoelectric absorption and by Thomson scattering in cold material, plus an iron emission line at 6.7 keV. We present the evolution of the spectral parameters with a temporal resolution of 16 s and show that the varying flux and spectrum can be interpreted solely by a time varying column density. The data do not appear to require non-solar abundances in the absorbing material, although a slight over-abundance of the metals cannot be ruled out. We also find that the lightcurve is characterized by symmetric substructures which can be successfully modeled by Gaussian profiles. The recurrence time of these substructures is on a timescale of a few minutes.

Key words: accretion, accretion disks – stars: neutron – X-rays: stars – stars: individual: Hercules X-1

1. Introduction

The study of transient dips in the X-ray lightcurves of X-ray binaries can help to provide insight into the accretion processes in these objects. The dips are thought to be caused by cold material with an appreciable column density of $10^{23}\,\mathrm{cm}^{-2}$ and higher passing through the line of sight to the neutron star. Since the dipping activity occurs primarily around the upper conjunction of the neutron star (i.e., shortly before the X-ray eclipse), this material is most probably due to the "splash" at the location where the accretion stream hits the accretion disk. A recent review on X-ray dip energy spectra has been published by White et al. (1995).

X-ray dips of the X-ray binary Her X-1 were first described by Giacconi et al. (1973). Two different kinds of dips are seen: pre-eclipse dips, which occur at orbital phases $\Phi_{\mathrm{orb}} = 0.7$–$1.0$, and anomalous dips, which are observed at $\Phi_{\mathrm{orb}} \sim 0.2$. During the "Main High" phase of the 35 d cycle of Her X-1, the pre-eclipse dips seem to "march" towards earlier orbital phases (Crosa & Boynton 1980; Giacconi et al. 1973). Interpretations of the marching behavior have been given in terms of a periodic mass transfer driven by the changing radiation pressure at the inner Lagrangian point (Crosa & Boynton 1980), and by the splash of the accretion stream onto a warped accretion disk (Schandl 1996). Note that the observational basis for the "marching behavior" has recently been challenged by Leahy (1997).

Previous observational studies dedicated to pre-eclipse dips of Her X-1 have been presented by Ushimaru et al. (1989), Choi et al. (1994), Leahy et al. (1994), and Reynolds & Parmar (1995). These authors found that the dip spectra can be modeled by a temporally variable absorption of the non-dip spectrum. In addition to this absorption component, a further weak unabsorbed component is present during the dips, as first seen in Tenma data (Ushimaru et al. 1989) and verified by later observations. This component has been interpreted as being due to Compton scattering of the primary neutron star radiation by an extended corona into our line of sight. Although the unabsorbed component always contributes to the observed X-ray spectrum, it can only be identified during dips and during the "low state" of Her X-1 (Mihara et al. 1991). Due to the comparably small effective areas of the earlier instruments, a study of the detailed temporal evolution of the spectral parameters during a dip has not been possible in these observations. Therefore, earlier investigators were forced to combine data obtained during (non-consecutive) time intervals with similar measured count-rates to obtain spectra with a signal to noise ratio sufficient for spectral analysis. This approach is not without problems, however, since a strong variation of N_{H} during the time intervals used for accumulating the spectra can lead to spurious spectral features like an apparent decrease in the flux incident onto the absorbing material (Parmar et al. 1986).

To be able to resolve the structures occuring on short timescales, instruments with a larger effective area and moderate energy resolution are needed. In this paper, therefore, we present results from the analysis of an RXTE observation of Her X-1,

Send offprint requests to: B. Stelzer

⋆ Table 2 is only available in electronic form at the CDS via anonymous ftp to cdsarc.u-strasbg.fr (130.79.128.5) or via http://cdsweb.u-strasbg.fr/Abstract.html.

⋆⋆ *Present address:* Max Planck Institut für Extraterrestrische Physik, Giessenbachstr. 1, D-85740 Garching bei München
Correspondence to: B. Stelzer

focusing on the spectral analysis and the behavior of the lightcurve during a pre-eclipse dip. Results from a previous analysis of these data, focusing on the orbit determination, have been presented by Stelzer et al. (1997). In Sect. 2 we describe our RXTE observation and the data reduction. Sect. 3 presents our results on the temporal evolution of the column density of the absorbing material throughout the dip, using two different data analysis methods. In Sect. 4 we discuss the temporal behavior of the source in terms of a simple model for individual structures in the lightcurve. We summarize our results in Sect. 5.

2. Observations and data analysis

Our RXTE observations of Her X-1 were performed on 1996 July 26. We primarily use data obtained with the PCA, the low energy instrument onboard RXTE. The PCA consists of five nearly identical Xe proportional counters with a total effective area of about $6500\,\mathrm{cm}^2$ (Jahoda et al. 1997). The data extraction has been performed using the RXTE standard data analysis software, ftools 4.0. To avoid contamination of the spectra due to the Earth's X-ray bright limb, only data measured at source elevations more than 10° above the spacecraft horizon were used in the present analysis. Background subtraction was performed with version 1.5 of the background estimator program, using a model where the background is estimated from the rate of Very Large Events in the detector. The diffuse X-ray background and a model for the activation of radioactivity within the detector is added. See Jahoda (1996) for a description of the PCA.

For the spectral analysis, version 2.2.1 of the PCA response matrix was used (Jahoda, 1997, priv. comm.). The spectral modeling of data from an observation of the Crab pulsar made available to us by the RXTE PCA and HEXTE teams with this matrix suggests that the matrix is well understood on the 1% level (see Dove et al. 1998 for a discussion of these data). Using this version of the PCA response matrix, the overall description of the Crab continuum is good, with the remaining deviations mainly being below 3 keV and around the Xe K edge at 35 keV. To avoid these uncertainties we used data from 3 to 18 keV only, which is sufficient for an analysis of the dips because of the power law nature of the Her X-1 X-ray spectrum and due to the E^{-3} dependency of the photoionization cross section (see discussion in Sect. 3.2). To obtain meaningful χ^2 values and to take into account the remaining uncertainties of the matrix, we added a 1% systematic error to all PCA channels. The spectral analysis was performed with XSPEC, version 10.00p (Arnaud 1996).

3. Time evolution of spectral parameters

3.1. Dip lightcurves

The full lightcurve of the July 26 pre-eclipse dip is shown in Fig. 1. Gaps in the data stream are due to passages through the South Atlantic Anomaly and due to the source being below the spacecraft horizon. The dip ingress, which occurred at orbital phase $\Phi_{\mathrm{orb}} = 0.75$, is characterized by a rapid decrease in intensity by a factor 3 within 80 s. The RXTE observation corresponds to a 35 d phase of $\Psi_{35} \sim 0.13$, that is the observation

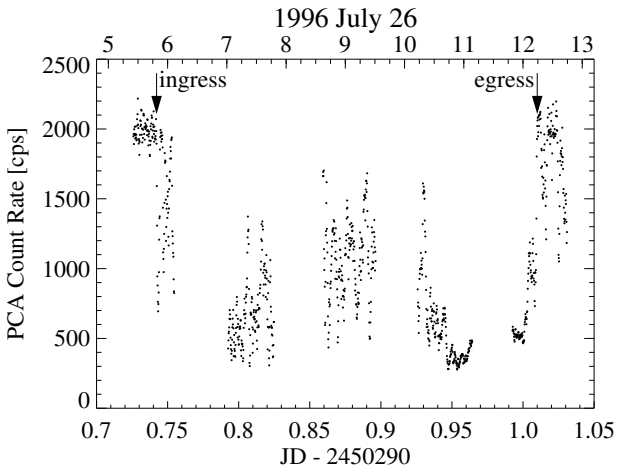

Fig. 1. Lightcurve during the dip of the RXTE observation in July 1996, 16 s resultion. Top x-axis: Time [UT]

took place 4 to 5 days after the Turn-On of the Main High State. From the behavior of the lightcurve in Fig. 1 we estimate that the dip egress takes place close to the end of the observation, when the count rate again reaches the pre-dip level. Under this assumption the duration of the dip was 6.5 hours.

In order to describe the time evolution of spectral parameters we use two complementary methods: First, we divide the whole dip lightcurve into segments of 16 s duration and perform spectral fits to each of these segments (Sect. 3.2). Secondly, we use color-color diagrams to model the time evolution of the column density (Sect. 3.3).

3.2. Spectral modeling

As was mentioned in Sect. 1, the common explanation for the dips is that of photoabsorption and scattering by foreground material. The photon spectrum ($\mathrm{ph\,cm^{-2}\,s^{-1}\,keV^{-1}}$) resulting from this process can be well described by a partial covering model of the form

$$N_{\mathrm{ph}} = E^{-\alpha} \cdot [I_{\mathrm{A}} \exp\left(-\left(\sigma_{\mathrm{T}} k N_{\mathrm{H}} + \sigma_{\mathrm{bf}}(E) N_{\mathrm{H}}\right)\right) + I_{\mathrm{U}}] + \mathrm{GAUSS} \quad (1)$$

where $\sigma_{\mathrm{bf}}(E)$ is the photoabsorption cross section per hydrogen atom (Morrison & McCammon 1983), σ_{T} is the Thomson cross section, and $k = N_{\mathrm{e}}/N_{\mathrm{H}}$ is the number of electrons per hydrogen atom (N_{e} is the electron column density). In Eq. (1), the continuum emission is modeled as the sum of two power laws, one of which is photo-absorbed by cold matter of column density N_{H}, as well as Thomson scattered out of the line of sight by electrons in the cold material. The second power law is not modified by the absorber, indicating that this additional (scattering) component comes from a geometrically much larger, extended region and thus is not affected by the photoabsorption. To this continuum, an iron emission line (described by a Gaussian) is added, which remains unabsorbed to simplify the spectral fitting process.

Two-component models similar to that of Eq. (1) have previously been shown to yield a good description of the dip spectra,

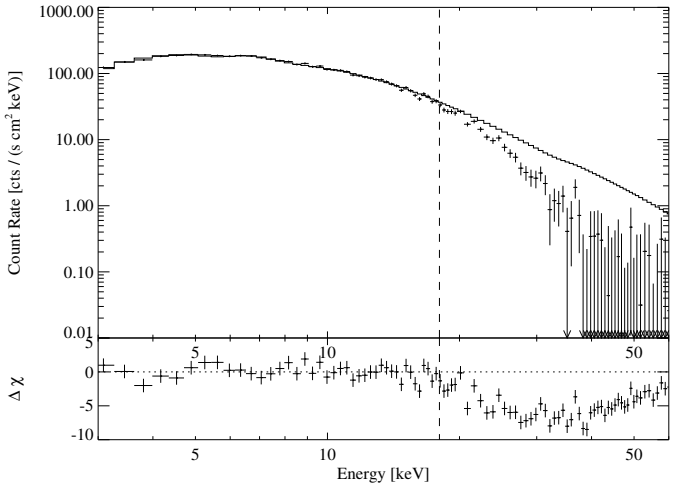

Fig. 2. 16 s PCA spectrum taken outside of the dip, modeled with the spectral shape from Eq. 1 over the energy interval used for our analysis of the dip-spectra. Significant deviations from the power-law continuum model appear only at energies above 18 keV, indicating that a power-law is sufficient in describing the data below 18 keV.

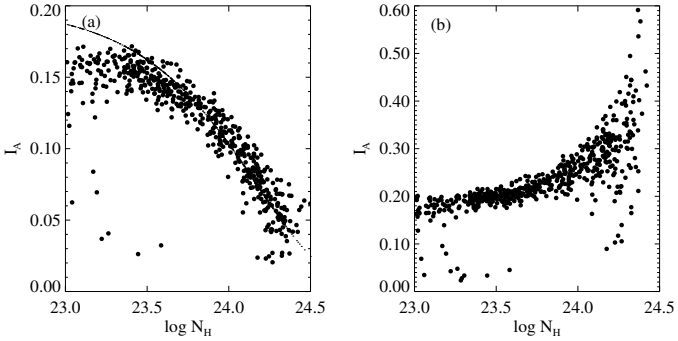

Fig. 3a and b. Dependency of the absorbed intensity I_A on the column density $N_{\rm H}$ for variations of the two component model: **a** model without inclusion of Thomson scattering, and **b** model with free I_A. In subfigure **a** the line represents the exponential Thomson factor $I_A \exp(-\sigma_{\rm T} N_{\rm H})$ for $I_A = 0.2\,\mathrm{ph\,cm^{-2}\,s^{-1}\,keV^{-1}}$. Uncertainties have been omitted for clarity.

while other simpler models were found to result in unphysical spectral parameters. As we mentioned in Sect. 2, to avoid response matrix uncertainties and problems with the exponential cutoff and the cyclotron resonance feature we include only data from 3 to 18 keV in our analysis. This approach results in a simpler spectral model than that used by Choi et al. (1994) and Leahy et al. (1994), who included the whole Ginga LAC energy band from 2 to 37 keV in their analysis. Since $\sigma_{\rm bf} \propto E^{-3}$, except for the highest values of $N_{\rm H}$, photoabsorption will virtually not influence the spectrum above $\sim$10 keV, such that the inclusion of data measured up to 18 keV is sufficient for the determination of the continuum strength. As we show in Fig. 2, neither the exponential cut-off nor the cyclotron resonance feature at $\sim$35 keV need to be taken into account when restricting the upper energy threshold to 18 keV, as significant deviations between the data and the model are observed only for energies above 18 keV. We, therefore, conclude that between 3 and 18 keV, additional continuum components do not affect the spectrum. When holding the power law index constant at its pre-dip value, from our spectral fits of the dip data we obtain acceptable χ^2 values ($\chi^2_{\rm red} \lesssim 1.5$). Introducing additional freedoms by leaving the photon index as a free parameter in the fit does not significantly improve the results. Therefore, we do not have to include high energy data to determine the continuum parameters.

In different attempts to fit the 16 s time resolved spectra without explicitly allowing for Thomson scattering of the absorbed component we found that the absorbed intensity which was then a free parameter was strongly anticorrelated with the column density. The relation between $I_{\rm A}$ and $N_{\rm H}$ from a fit of a spectral model that does not take account of Thomson scattering is shown in Fig. 3 a. The observed anticorrelation reflects the exponential $N_{\rm H}$-dependence of the Thomson scattering factor and led us to the conclusion that absorption and Thomson scattering may not be separated. We, therefore, use the model of Eq. (1) and hold the continuum parameters fixed to their measured pre-dip values: a single power law of photon index 1.06 plus an emission line feature from ionized iron at 6.7 keV with width of $\sigma = 0.46$ keV ($\chi^2_{\rm red} = 1.1$ at 3–18 keV for 30 degrees of freedom). The normalization of the absorbed power law, $I_{\rm A}$, was also fixed to its pre-dip value, $I_{\rm A} = 0.20\,\mathrm{ph\,cm^{-2}\,s^{-1}\,keV^{-1}}$. Finally, the ratio $k = N_{\rm e}/N_{\rm H}$ was set to 1.21, appropriate for material of solar abundances. We emphasize that fixing the parameters to their normal state values assumes that the intrinsic spectral shape of the source does not change during the dip and that variations of the observed spectrum are due to the varying column density only. This is justified by the apparent constancy of the lightcurve outside the dip. Particularly, if $I_{\rm A}$ is free in the fit, we observe an increase of this parameter for very high $N_{\rm H}$, which is not clearly systematic (see Fig. 3 b). Such a correlation between $I_{\rm A}$ and $N_{\rm H}$ seems to indicate an additional dependence of $I_{\rm A}$ on the column density (next to the Thomson scattering already taken into consideration in the spectral model). Rather than being due to real variations of the absorbed intensity, we consider this relation to be produced artificially by the fitting process: Variations of $I_{\rm A}$ during the dip might come about as compensation for slight misplacements of the column density. Any remaining correlation in Fig. 3 b might contain a possible contribution from slight variations in the absorbed continuum. Due to the limited energy resolution of the detector, however, $N_{\rm H}$ and α are strongly correlated. Therefore, a slight real variation is not convincingly separable from the artificial one.

To summarize, the remaining free parameters of the spectral model are the iron line normalization, $N_{\rm Fe}$, the normalization of the unabsorbed component, $I_{\rm U}$, and the column density, $N_{\rm H}$.

We divide the dip observation into 16 s intervals and obtain 941 spectra, covering the energy range from 3 to 18 keV. After subtracting the background, which has been modeled on the same 16 s basis, the individual spectra were fitted with the model of Eq. (1). Typical $\chi^2_{\rm red}$ values obtained from these fits are between 0.5–1.5 for 37 degrees of freedom, indicating that our simple spectral model is sufficient to describe the data.

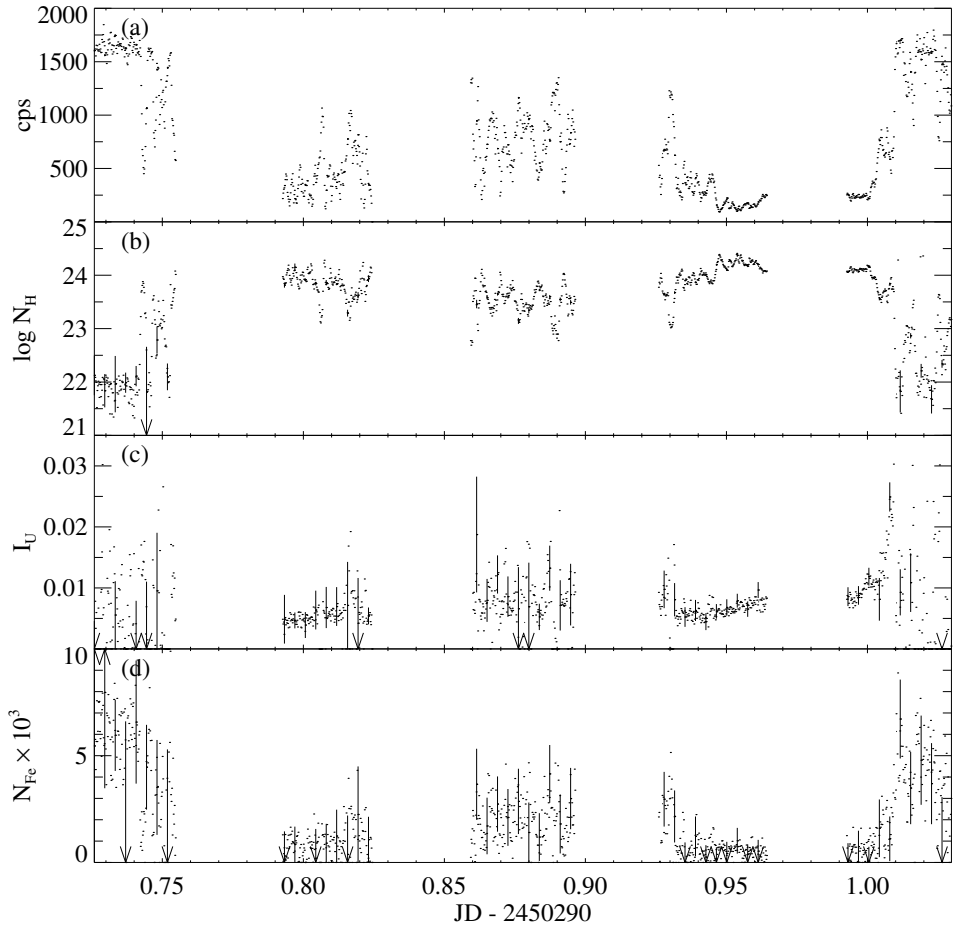

Fig. 4a–d. Time evolution of bestfit parameters from spectral fitting in 16 s intervals: **a** PCA count rate for the energy interval from 3.5 to 17 keV, **b** $\log N_{\rm H}$, where $N_{\rm H}$ is measured in cm^{-2}, **c** normalization of the unabsorbed power law, $I_{\rm U}$, in $\mathrm{ph\,cm^{-2}\,s^{-1}\,keV^{-1}}$ at 1 keV, **d** normalization of the Gaussian emission line. Uncertainties shown are at the 90% level for one parameter. For clarity, the error bars are only shown for every 20th data point.

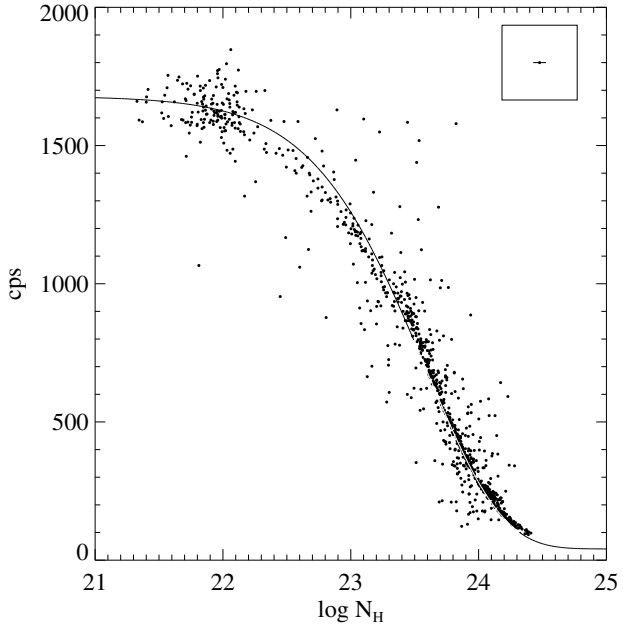

Fig. 5. PCA count rate in the band from 3 to 18 keV as a function of the measured column density. The line represents the count rates predicted by the model of Eq. (1). Inset: typical $1\,\sigma$ uncertainty for $N_{\rm H}$.

The temporal behavior of the column density mirrors that of the lightcurve (Figs. 4a and b). This supports the assumption that the underlying cause for both is absorbing material whose presence in the line of sight blocks off the X-ray source and thus leads to a modification of the spectral shape due to energy dependent absorption and energy independent scattering as well as a corresponding reduction in the 3 to 18 keV flux. The highest value measured for the column density is about $3\,10^{24}\,\mathrm{cm}^{-2}$, comparable to that found in previous measurements (Reynolds & Parmar 1995). The variation of the measured count rate with $N_{\rm H}$ is shown in Fig. 5 together with the count rates predicted by our partial covering model. The transition from the dip to the normal state is manifested in the break of the slope around 1500 cps. The figure indicates that due to the 3 keV energy threshold of the PCA, the instrument is sensitive only to values of $N_{\rm H}$ of about $5\,10^{22}\,\mathrm{cm}^{-2}$ and above. This also explains why we measure $N_{\rm H} \simeq 10^{22}\,\mathrm{cm}^{-2}$ for the out-of-dip data just before dip-ingress, a value which is rather high compared to the value for absorption by the interstellar medium along the line of sight ($1.7\,10^{19}\,\mathrm{cm}^{-2}$, Mavromatakis 1993).

The normalization of the unabsorbed component, $I_{\rm U}$, is found to stay almost constant during the whole dip, indicating that the whole variability of Her X-1 during the dip is due to absorption and scattering in the intervening material. The absolute value of $I_{\rm U}$ is quite small (about 2.5% of $I_{\rm A}$).

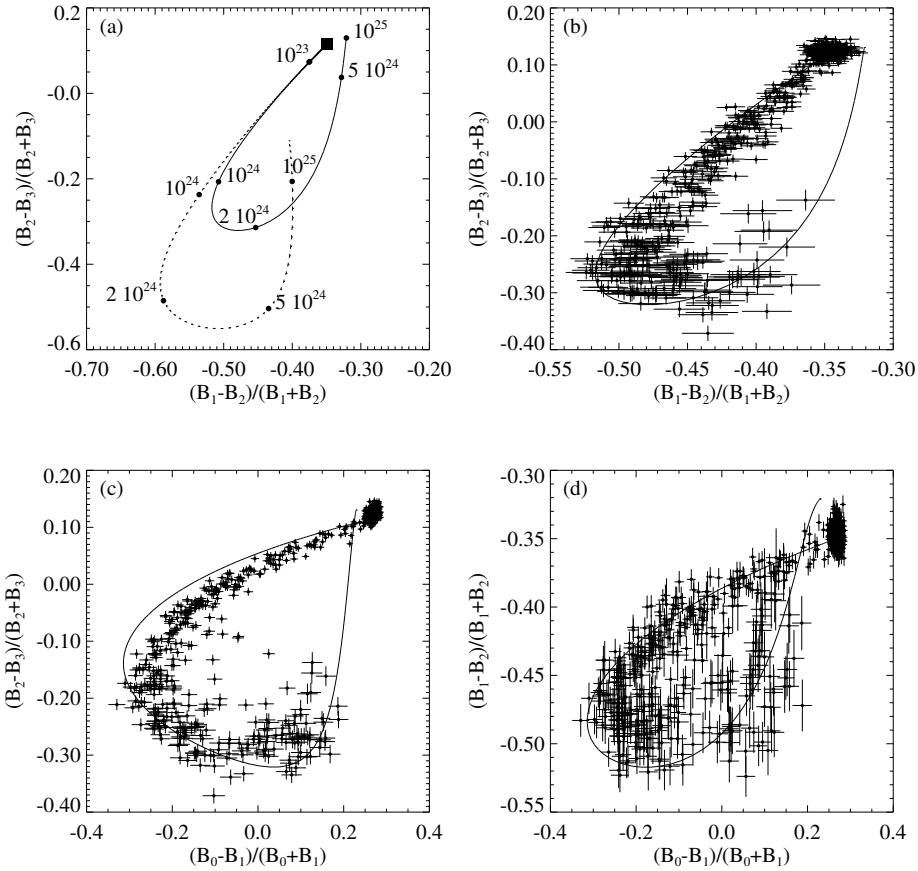

Fig. 6. a Theoretical track of a partial covering model (solid line) and a model without unabsorbed component (dashed line) in a color color diagram for spectral parameters typical for Her X-1. Labels on the curve refer to column densities (in cm^{-2}). **b–d** Color-color diagrams and best fit partial covering models for the dip of the RXTE observation.

Table 1. Energy bands defined for the analysis of colors.

Band	Energy [keV]	PHA Channels
B_0	3– 5	4–11
B_1	5– 7	12–15
B_2	7–11	16–26
B_3	11–17	27–42

The normalization of the iron line, N_{Fe}, also shows some decline during phases of high column density. Note, however, that in our spectral model the line feature is not absorbed and scattered. The remaining variation can in principle be explained by partial covering of the line emitting region.

3.3. Color-color diagrams

As an alternative to spectral fitting, the development of the column density can be visualized by color-color diagrams which show the behavior of broad band X-ray count rates (cf. Leahy 1995 for earlier results from Ginga data). We define four energy bands covering approximately the same range as our spectral analysis (Table 1). We then define modified X-ray colors by $(B_0 - B_1)/(B_0 + B_1)$, $(B_1 - B_2)/(B_1 + B_2)$, and $(B_2 - B_3)/(B_2 + B_3)$ where B_i is the count rate in band i. For any given spectral model, a theoretical color can be obtained by folding the spectral model through the detector response matrix. If the only variable parameter in the model is N_{H}, the resulting colors are found to trace characteristic tracks in the color-color diagram. Comparing these tracks with the measured data it is possible to infer the temporal behavior of the column density (see below).

As an example, Fig. 6a displays typical theoretical tracks for two possible spectral models for Her X-1. The dotted track represents a model without an unabsorbed component (called the one-component model henceforth), while the solid line is the track computed for a partial covering model. The form of this partial covering model is identical to Eq. (1) with the exception that the iron line is also absorbed and scattered. We used photoabsorption cross sections from Verner & Yakovlev (1995) and Verner et al. (1996) in the computation of the diagrams. The difference between these cross sections and those from Morrison & McCammon (1983) used in Sect. 3.2 is negligible, though. The typical shape of the tracks is due to the E^{-3} proportionality of the absorption cross section σ_{bf}: for low values of N_{H} only the lower bands are influenced by the absorbing material, while for high values of N_{H} all bands are influenced. In both cases the model track starts at the low N_{H}-values in the upper right corner of the diagram marked by the square which describes the situation before the dip. Moving along the track the column density increases. For low values of N_{H}, the tracks of both models are similar since the influence of absorption is negligible. For larger N_{H} the lower energy bands are increasingly affected by absorption. At a critical value of N_{H} the unabsorbed

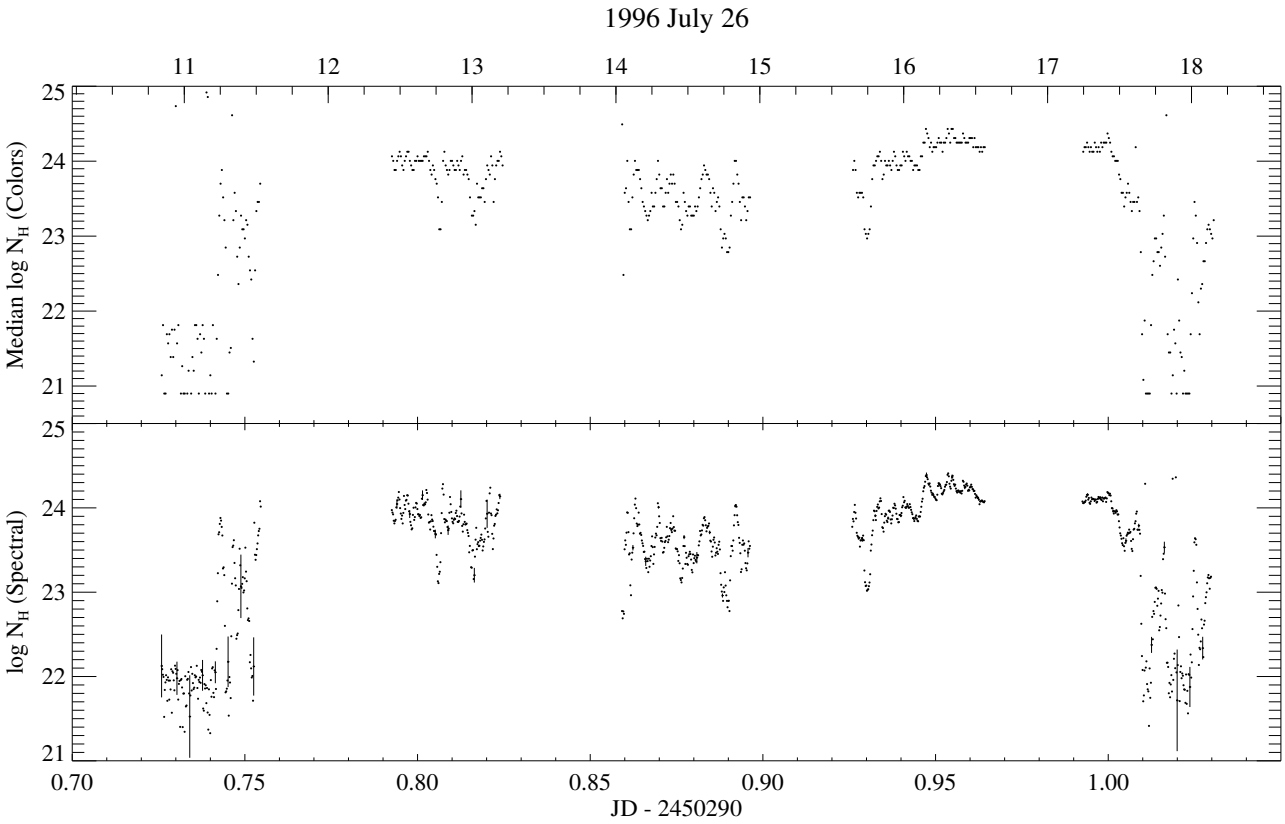

Fig. 7. Comparison of the time development of $N_{\rm H}$ as found from different methods: *Upper panel:* $N_{\rm H}$ from color-color diagrams, *lower panel:* $N_{\rm H}$ from spectral fitting.

component begins to dominate the low energy bands in the partial covering model. Since the unabsorbed component has, by definition, the same shape as the non-dip spectrum, the track turns towards the low-$N_{\rm H}$ color. In the one-component model, the absence of an unabsorbed component leads to a further decrease in flux in the low energy bands that is only stopped by response matrix and detector background effects.

For each of the energy bands defined in Table 1 we generate a background subtracted lightcurve of 32 s resolution and obtain the color-color diagrams shown in Fig. 6b–d. The data line up along a track which is curved similar to the theoretical tracks of Fig. 6a. The accumulation of data points in the upper right corner of the diagrams of Fig. 6b–d consists of the out-of-dip data, where the colors remain constant and the column density is at its lowest value. As noted above, the early turn of the observed tracks in the color-color diagram suggests the presence of an unabsorbed spectral component in the data. To quantify this claim, we compare theoretical tracks from the partial covering model to the data. This is done by varying the relative contributions of $I_{\rm A}$ and $I_{\rm U}$ to the total spectrum such that the total normalization of the incident spectrum, $I_{\rm A} + I_{\rm U}$, is kept at its pre-dip value. Except for the normalizations, all other spectral parameters are fixed at their pre-dip values (cf. Sect. 3.2). We define the best fit model to be the model in which the root mean square distance between the track and the data is minimal (cf. Fig. 6). Not surprisingly, the ratio between $I_{\rm A}$ and $I_{\rm U}$ found using this method is similar to the average ratio found from spectral fitting, about 3%.

Using this best fit model, $N_{\rm H}$ as a function of time is found by projecting the measured colors onto the track. The projection provides slightly different values of $N_{\rm H}$ for each color-color diagram examined. Major discrepancies are due to projection onto a wrong part of the model curve in the region where the curve overlaps with itself. To even out these discrepancies we calculated the median of $N_{\rm H}$ from all three color-color diagrams used in our analysis. The time development of $N_{\rm H}$ found from the color-color diagrams is in good agreement with the $N_{\rm H}$ resulting from the spectral fits (Fig. 7).

4. Light curves

The irregular variations observed in the lightcurve during the dips are generally thought to be due to the cloudy structure of an absorber extending above the disk surface. The location of the material, i.e., its distance from the neutron star, however, is unknown and depends on model assumptions. According to Crosa & Boynton (1980), the obscuring matter is the temporarily thickened disk rim, or, in the modification of this model by Bochkarev (1989) and Bochkarev & Karitskaya (1989), consists of "blobs" in an extended corona above the disk rim. On the other hand, in the coronal wind model of Schandl et al. (1997) the dips are caused by a spray of matter at some inner disk radius where the accretion stream impacts on the disk.

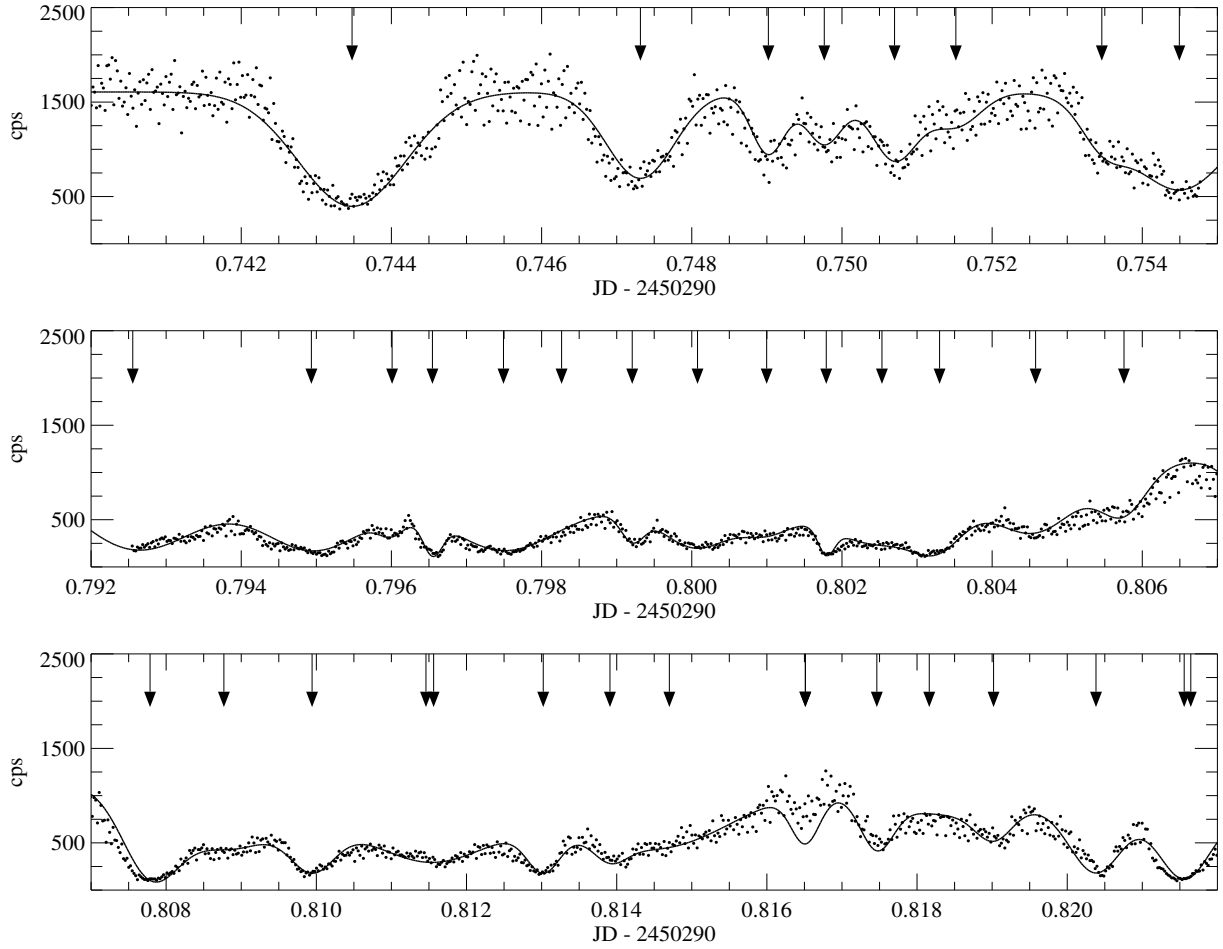

Fig. 8. Gaussian fits to the dip lightcurve with a temporal resolution of 2 s. Arrows mark the position of Gaussian line centroids.

Since all models assume that the absorbing matter exists in the form of clumps of material, it is interesting to ask whether these blobs can be seen in the data. The symmetry of the structures in the first half of the lightcurve shown in Fig. 4a suggests that this is indeed the case. We therefore tried to model this part of the dip lightcurve by fitting Gaussians to each of the visibly identified structures. The best fit to the data is displayed in Fig. 8. Information about the parameters of each Gaussian is summarized in Table 2 (available in electronic form only). Note that the structures appear to be quasi-periodic on a time-scale of about 10^{-3} d (=90 s) which could provide a hint on their nature. A similar 144 s periodicity has previously been reported by Leahy et al. (1992). A study of a larger sample of dips is necessary, however, before any claim on the existence of periodic structures in the dip data can be settled.

Assuming that each structure in the lightcurve represents a single cloud of matter which is absorbing X-rays while crossing the line of sight, the width of the Gaussian represents a direct measure of the crossing time for such a cloud. The horizontal extent of the cloud could be derived if the radial distance of these clouds from the neutron star and their velocity were known. To give a rough estimate for the cloud size, we assume that the matter moves on Keplerian orbits close to the outer disk rim (as is favored by the model of Crosa & Boynton 1980), at a distance of $2\,10^{11}$ cm from the neutron star (Cheng et al. 1995). The Keplerian velocity at this radius is approximately $3\,10^{7}\,\mathrm{cm\,s^{-1}}$. Assuming that the clouds are spherical, i.e., assuming that their angular size estimated from the FWHM of the fitted Gaussian corresponds to their radial size, we derive typical cloud diameters on the order of $10^{8\ldots10}$ cm. Making use of the observed column densities we find a proton density of about $6\,10^{14}\,\mathrm{cm^{-3}}$. On the other hand, the apparent periodicity mentioned above might also indicate that the blobs are very close to the neutron star. Assuming Keplerian motion, the periodicity could indicate orbital radii as small as 10^{9} cm (the inner radius of the accretion disk is at 10^{8} cm; Horn 1992) and their densities would be accordingly higher.

5. Discussion and conclusions

In this paper we have presented the temporal evolution of spectral parameters of Her X-1 during a pre-eclipse dip. Due to the large effective area of the PCA, the temporal resolution of our data is higher than that of earlier data. Using two different methods we were able to show that a partial covering model in which the column density N_{H} and the normalization of the unabsorbed continuum I_{U} are the only time variable spec-

tral components is sufficient to explain the observed spectral and temporal variability. This result is in qualitative agreement with the previous analyses for pre-eclipse dips presented by Ushimaru et al. (1989), Choi et al. (1994), Leahy et al. (1994), and Reynolds & Parmar (1995). Note that models without an unabsorbed component were not able to result in satisfactory fits, which is also consistent with the low state observations presented by Mihara et al. (1991) where the unabsorbed component was clearly required. As proposed by Choi et al. (1994) from the analysis of the pulsed fraction of the lightcurve, the unabsorbed component is probably due to scattering of radiation in an extended hot electron corona into the line of sight. These authors also show that the interpretation of Ushimaru et al. (1989), who attributed the unabsorbed component to a leaky cold absorber, does not hold.

The anticorrelation between $I_{\rm U}$ and $N_{\rm H}$ found by Leahy et al. (1994) and Leahy (1997) in Ginga observations has been interpreted by these authors as evidence that the obscuring material partially also obscures the extended corona. Thus, the geometric covering fraction of the obscuring material is assumed to be quite high during episodes of large $N_{\rm H}$. Our measured values of $I_{\rm U}$ exhibit some variability (Fig. 4c), but there is no systematic correlation between $I_{\rm U}$ and $N_{\rm H}$, neither has such a correlation been seen by Choi et al. (1994). A possible interpretation for this discrepancy is that Leahy et al. (1994) and Leahy (1997) did not include Thomson scattering in their fits. Indeed, when setting $k = 0$ in Eq. (1) and fitting the RXTE data with both normalizations as free parameters, $I_{\rm U}$ is much more variable and $I_{\rm A}$ appears to be correlated with $N_{\rm H}$. In addition, it is generally difficult to distinguish between the absorbed and the unabsorbed component for low values of $N_{\rm H}$ such that $I_{\rm U}$ and $I_{\rm A}$ get easily confused by the fitting routine.

We also tried fitting the data with a spectral model in which $I_{\rm U}$ was held fixed at 0.005 ph cm^{-2} s^{-1} keV^{-1}, the average value of the fits of Sect. 3.2. The resulting $\chi^2_{\rm red}$ values from this fit were comparable to those of the fits presented in Sect. 3.2 since the variations in $I_{\rm U}$ in the latter fit are small enough to be compensated by slight changes in $N_{\rm H}$ in the former. Furthermore, due to the lower temporal resolution of the previous observations, small variations of $N_{\rm H}$ could not be resolved in these data. It has been pointed out by Parmar et al. (1986), that this effect might result in a large uncertainty in the determination of $I_{\rm U}$. As is shown by our fits to structures in the lightcurve (Fig. 8), we are able to resolve and identify individual structures with a temporal resolution of about one minute. Thus we are confident that the investigation presented here is unaffected by these problems.

In our analysis of Sect. 3.2 and 3.3 we assumed that $N_{\rm e}/N_{\rm H} = 1.21$, i.e., the value appropriate for material of solar composition. Previous investigations of dipping sources, however, hinted at non-solar abundances in most of these systems (Reynolds & Parmar 1995, White et al. 1995). A direct measurement of the abundance ought to be possible by fitting the RXTE data with a partial covering model in which $N_{\rm e}$ and $N_{\rm H}$ are both free parameters. We find that the average $N_{\rm e}/N_{\rm H} = 1.5$. Thus, our data could be interpreted as pointing towards a metal overabundance. In contrast to this result, a metal underabundance is favored by Reynolds & Parmar (1995)[1]. This discrepancy might be due to the higher temporal resolution of our data, where small variations of $N_{\rm e}$ can be traced. Note, however, that our method of determining $N_{\rm e}/N_{\rm H}$ depends crucially on the assumption that the spectrum incident on the absorbing cloud is constant over time and also depends strongly on the value adopted for $I_{\rm A}$. Although it is very probable that the source is constant (Sect. 3.2), slight variations of $I_{\rm A}$ cannot be ruled out. Therefore, we decided to use the solar value of 1.21 in our analysis and postpone the detailed study of the abundances until a larger sample of dips has been observed with RXTE.

To conclude, photoabsorption and electron scattering of photons out of the line of sight in cold material appear to be solely sufficient for explaining the temporal variability of the observed flux during this pre-eclipse dip of Her X-1. Further observations of a larger sample of pre-eclipse dips are necessary to verify this result.

Acknowledgements. We acknowledge W. Heindl, I. Kreykenbohm, and R. Meier for useful discussions on the data analysis. We thank G. Morfill and R. Neuhäuser for granting the first author the time to finish this work. This work has been financed by DARA grant 50 OR 92054.

References

Arnaud K.A., 1996, In: Jacoby J.H., Barnes J. (eds.) Astronomical Data Analysis Software and Systems V. Astron. Soc. Pacific, Conf. Ser. 101, Astron. Soc. Pacific, San Francisco, p. 17
Bochkarev N.G., 1989, SvA 33, 638
Bochkarev N.G., Karitskaya E.A., 1989, Ap&SS 154, 189
Cheng F.H., Vrtilek S.D., Raymond J.C., 1995, ApJ 452, 825
Choi C.S., Nagase F., Makino F., et al., 1994, ApJ 422, 799
Crosa L., Boynton P.E., 1980, ApJ 235, 999
Dove J.B., Wilms J., Nowak M.A., et al., 1998, MNRAS 298, 729
Giacconi R., Gursky H., Kellogg E., et al., 1973, ApJ 184, 227
Horn S., 1992, Dissertation, Ludwig-Maximilians-Universität München
Jahoda K., 1996, Estimating the Background in the PCA, Technical report, NASA GSFC, Greenbelt version dated November 27, 1996
Jahoda K., Swank J.H., Giles A.B., et al., 1997, In: Siegmund O.H. (ed.) EUV, X-Ray, and Gamma-Ray Instrumentation for Astronomy VII. Proc. SPIE 2808, SPIE, Bellingham, WA, p. 59
Leahy D.A., 1995, A&AS 113, 21
Leahy D.A., 1997, MNRAS 287, 622
Leahy D.A., Yoshida A., Kawai N., Matsuoka M., 1992, In: Shrader C.R., Gehrels N., Dennis B. (eds.) The Compton Observatory Science Workshop. NASA CP 3137, p. 193
Leahy D.A., Yoshida A., Matsuoka M., 1994, ApJ 434, 341
Mavromatakis F., 1993, A&A 273, 147
Mihara T., Ohashi T., Makishima K., 1991, PASJ 43, 501
Morrison R., McCammon D., 1983, ApJ 270, 119

[1] Note that Reynolds & Parmar (1995) assume that for material of cosmic abundance $N_{\rm e}/N_{\rm H} = 1$, and call the reciprocal of the measured ratio the "abundance". This reciprocal should not be confused with the common usage of abundance in astronomy since it ignores that the scattering cross section of an element with nuclear charge number Z is $Z\sigma_{\rm T}$.

Parmar A.N., White N.E., Giommi P., Gottwald M., 1986, ApJ 308, 199
Reynolds A.P., Parmar A.N., 1995, A&A 297, 747
Schandl S., 1996, A&A 307, 95
Schandl S., König M., Staubert R., 1997, In: Dermer C.D., Strickman M.S., Kurfess J.D. (eds.) Proc. 4th Compton Symposium, AIP Conf. Proc. 410, Woodbury: AIP, p. 763
Stelzer B., Staubert R., Wilms J., Geckeler R.D., 1997, In: Dermer C.D., Strickman M.S., Kurfess J.D. (eds.) Proc. 4th Compton Symposium, AIP Conf. Proc. 410, Woodbury: AIP, p. 753
Ushimaru N., Tawara Y., Koyama K., Hayakawa S., 1989, PASJ 41, 441
Verner D.A., Yakovlev D.G., 1995, A&AS 109, 125
Verner D.A., Ferland G.J., Korista K.T., Yakovlev D.G., 1996, ApJ 465, 487
White N.E., Nagase F., Parmar A.N., 1995, In: Lewin W.H.G., van Paradijs J., van den Heuvel E.P.J. (eds.) X-Ray Binaries. Cambridge Univ. Press, Cambridge, p. 1